REPORT DOCUMENTATION PAGE

Form Approved
OMB No. 0704-0188

1. REPORT DATE *(DD-MM-YYYY)*	**2. REPORT TYPE**	**3. DATES COVERED** *(From - To)*
3/31/10	Annual Performance Report	July 1, 2008 – July 1,2009

4. TITLE AND SUBTITLE
Active Plasmonics, Option 3 Report

5a. CONTRACT NUMBER

5b. GRANT NUMBER
FA9550-06-1-0480

5c. PROGRAM ELEMENT NUMBER

6. AUTHOR(S)
Harry A. Atwater

5d. PROJECT NUMBER

5e. TASK NUMBER

5f. WORK UNIT NUMBER

7. PERFORMING ORGANIZATION NAME(S) AND ADDRESS(ES)

California Institute of Technology
1200 E. California Blvd.
Pasadena, CA 91125

8. PERFORMING ORGANIZATION REPORT NUMBER

9. SPONSORING / MONITORING AGENCY NAME(S) AND ADDRESS(ES)

Air Force Office of Scientific Research
801 N. Randolph St Room 732
Arlington, VA 22203

Dr. Gernot S. Pomrenke
AFOSR/NE (703) 696-8426
Gernot.Pomrenke@afosr.af.mil

10. SPONSOR/MONITOR'S ACRONYM(S)

11. SPONSOR/MONITOR'S REPORT NUMBER(S)

12. DISTRIBUTION / AVAILABILITY STATEMENT A

13. SUPPLEMENTARY NOTES

14. ABSTRACT

Over the third year of the grant, our research program in active plasmonics has concentrated on developing ultracompact all-optical and electro-optic modulators based on metal-insulator-metal Fabry-Perot resonators. Highlights over the past year include

- Realization of tunable color filter pixels based on plasmonic metal-insulator-metal waveguides
- Demonstration of a plasMOStor, a Si CMOS plasmonic electro-optic modulator.

Another significant development was the collaborative work (with Yariv and Scherer groups at Caltech) of an electrically pumped hybrid evanescent Si/InGaAsP laser. Diest and Atwater developed the InP/Si bonding technology needed to realize active electrically pumped InP-based lasers on Si.

15. SUBJECT TERMS

16. SECURITY CLASSIFICATION OF:			**17. LIMITATION OF ABSTRACT**	**18. NUMBER OF PAGES**	**19a. NAME OF RESPONSIBLE PERSON**
a. REPORT	**b. ABSTRACT**	**c. THIS PAGE**			**19b. TELEPHONE NUMBER** *(include area code)*

Standard Form 298 (Rev. 8-98)
Prescribed by ANSI Std. Z39.18

Status of Effort:

Over the third year of the grant, our research program in active plasmonics has concentrated on further developing ultracompact plasmostor electro-optic modulators based and also color filter pixels based on modulation of the complex refractive index for surface plasmon polaritons in nanoscale two-dimensional Fabry-Perot resonators. Highlights over the past year include

- Demonstration of a SOI waveguide-coupled plasmostor, i.e., an SOI waveguide-coupled Si CMOS plasmonic electro-optic modulator. By cladding an SOI waveguide with an MIM plasmon waveguide, electro-optic modulation of up to 4 dB is achieved in device volumes of half of a cubic wavelength with femtojoule switching energies and the potential for GHz modulation frequencies.
- Development of an MIM waveguide based color filter pixel. The pixel filters white light and transmits colors based on waveguide transverse and longitudinal mode number. We also investigated the possibility of color-switching via electro-optic modulation using $LiNbO_3$ as the insulator section of a metal-insulator-metal active waveguide device, and we identified the range of color change possible by electro-optic switching of such an electro-optic MIM color filter pixel.

Other work in year 3 included collaboration with the groups of Axel Scherer and Amnon Yariv to realize an electrically pumped hybrid Si-InGaAsP evanescent wave laser. Diest and Atwater developed the InP/Si bonding technology needed to realize active electrically pumped InP-based lasers on Si.

Future Plans

Our work on active plasmonics has led in several new directions. First, our collaboration is underway with CEA-LETI laboratory in Grenoble, France, to realize a plasmostor fabricated in a CMOS foundry process. We expect plasmostor wafer processing to be finished in mid-2010. Second, we have been investigating plasmonic enhancement of spontaneous emission in AlGaAs/GaAs nanowires and expect that results of this effort will be forthcoming in 2010.

Accomplishments/New Findings:

Plasmonic MIM Tunable Color Filter Pixels

Color filters are a key component in digital photography, digital projectors, and computer displays, and current research on color filtering is focused on developing smaller, faster, and lower power designs. One approach to meeting these challenges is the use of plasmonic resonators that couple incident light into electromagnetic modes that propagate along a metal-dielectric interface. Because of the ability to integrate electrodes in a straightforward manner, metal insulator-metal (MIM) waveguides are of considerable interest for electro-optic device applications.

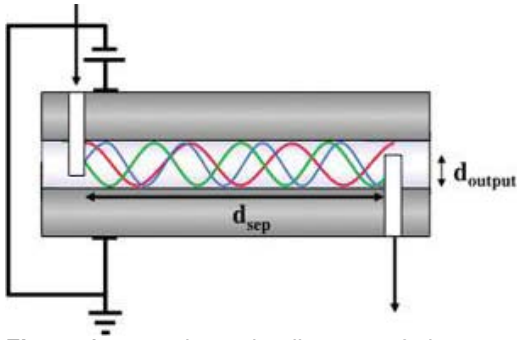

Figure 1. A schematic diagram of the MIM geometry used with input and output slits placed on the top and bottom of the waveguide (a). Depicted within the dielectric layer of (a) are the red, green, and blue photonic modes of the MIM waveguide. The spacing between input and output slits is labeled d_{sep}, and the output slit's depth into the dielectric layer is labeled as d_{output}.

We have developed a method for filtering white light into individual colors using metal-insulator-metal resonators. The resonators are designed to support photonic modes at visible frequencies, and dispersion relations are developed for realistic experimental configurations. Experimental results indicate that passive Ag/Si3N4/Au resonators exhibit color filtering across the entire visible spectrum. Full field electromagnetic simulations were performed on active resonators for which the resonator length was varied from 1-3 μm and the output slit depth was systematically varied throughout the thickness of the dielectric

layer. These resonators filter colors based on interference between the optical modes within the dielectric layer. By careful design of the output coupling, the resonator can selectively couple to intensity maxima of different photonic modes and, as a result, preferentially select any of the primary colors. We also showed how refractive index modulation in metal-insulator-metal resonators can yield actively tunable color filters. Simulations using lithium niobate as the dielectric layer and the top and bottom Ag layers as electrodes, indicate that the output color can be tuned over the visible spectrum with an applied field.

A schematic diagram of the MIM resonator geometry used is shown in Figure 1. This structure has input and output slits milled into the top and bottom cladding layers, respectively. The separation between the input and output slits is labeled "d_{sep}", and the depth to which the output slit is etched into the lithium niobate is labeled "d_{output}". Plane wave white light illumination in the wavelength range λ) 400-700 nm is sent through the input slit, traverses the length of the optical cavity, and is detected after exiting the output slit.

To calculate the color that an observer would observe at the device output, the CIE (1964) color matching functions are used to correlate the chromatic response of the color-sensitive cones within the observer's eye over the visible range of the MIM output spectrum. The red, green, and blue spectral sensitivity curves of the human eye are shown from 400-700 nm. The transmitted optical power spectrum through the output slit of each device was recorded. The resulting color output was calculated by taking the inner product of each of the R, G, and B color matching functions with the optical intensity from a specific device over the entire visible spectrum. Then color scales were developed that illustrated the output color seen by an observer.

Modeling the dispersion of the MIM waveguides shows the existence of the plasmonic and three photonic modes, as illustrated in Figure 2a, which is a plot of the frequency dependence of the real part of the wavevector. When the dielectric layer of the MIM waveguide is composed of lithium niobate, the MIM geometry facilitates electro-optic modulation of the refractive index. The coercive field for lithium niobate is ~4 kV/mm. Under an applied electric field greater than the coercive field, the lithium niobate was modeled as having a refractive index increase of ~0.12 across the visible spectrum, and the imaginary part of the index was kept the same as in the zero field case.

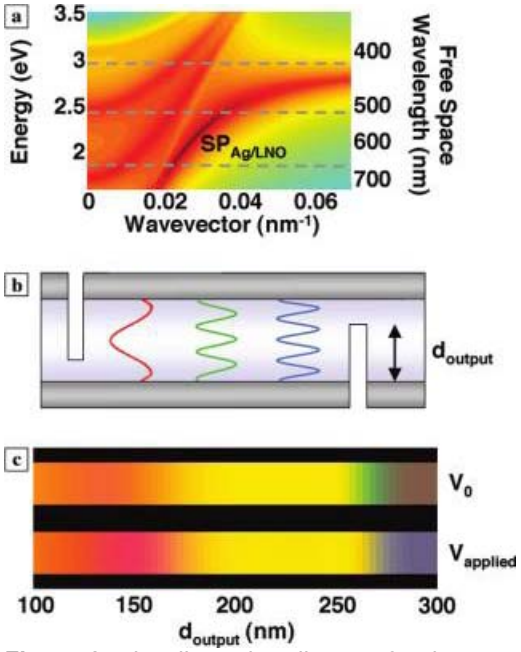

Figure 2. The dispersion diagram for the MIM structure with 300 nm of lithium niobate between two, 400 nm layers of silver, (a). The plot shows the plasmonic and three photonic modes that lie in the red, green, and blue regions of the visible spectrum. By adjusting the output slit depth, the device will selectively couple to the red, green, or blue photonic modes. These mode profiles are plotted within the MIM structure in (b). Not shown here is the mode profile of either the symmetric or antisymmetric plasmon mode. The resulting output colors from a MIM waveguide with an input-output slit spacing of 2000 nm are shown in (c). The top stripe of color is
for devices under no applied field and the bottom stripe is for devices under an applied field.

For a lithium niobate layer 300 nm thick, the dispersion calculations show that the structure's three photonic modes lie in the regions 1.9, 2.5, and 3 eV, which correspond to the red, green, and blue regions of the visible spectrum, respectively. Figure 2b shows the red, green, and blue photonic mode profiles moving through the MIM waveguide. Not shown here is the mode profile of either the symmetric or antisymmetric plasmon modes. The MIM waveguides modeled in Figure 2c had a constant d_{sep} = 2000 nm for all devices with and without an applied electric field. For these simulations, d_{output} was increased from 100-300 nm into the lithium niobate in 2 nm increments from one colored panel to another in Figure 2c. By simply varying the depth of the output slit into the lithium niobate layer, one can preferentially couple to the different photonic modes and output any of the primary colors. In Figure 2c, the top color stripe corresponds to no applied electric field and the bottom color stripe corresponds to devices under an applied field. For these specific devices, the output slit most efficiently couples to the red mode with and without an applied electric field for slit depths below □150 nm. With no applied electric field, the output slit most efficiently couples to the green mode between 250 and 275 nm, and with an applied field the output slit most efficiently couples to the blue mode above ~285 nm.

PlasMOStor: Si CMOS Plasmonic Electro-Optic Modulator

Use of plasmonic components offers a unique opportunity for addressing the size mismatch between electrical and optical components. In terms of integrating standard Si-based electronics with Si-based photonics, it would be highly desirable to develop a suite of plasmonic devices with Si as the active medium. This approach would allow for compatibility with standard CMOS processing techniques and potential integration into existing Si-based photonic networks. Unfortunately, unstrained Si exhibits an indirect bandgap and no linear electro-optic effect, yielding a continuous-wave optical response that is typically either slow or weak. However the refractive index can be modulated in plasmonic MIM waveguides by carrier accumulation and depletion, and this is the basis of the plasmostor that was developed in Performance Period 2.

In Performance Period 3, we expanded upon the experimental demonstration of the plasmostor achieved in Period 2. Like the Si-based modulators implemented by Lipson and colleagues at Cornell, this device utilizes high optical mode confinement to enhance electro-optical nonlinearities in Si. Moreover, like the Si optical modulator of Liu and colleagues at Intel, this device exploits the fast modulation of accumulation conditions in a metal-oxide-semiconductor (MOS) capacitor. In contrast with these structures, our plasmonic modulator achieves modulation of over 11 dB *in device volumes of half a cubic wavelength*. In particular, our device illustrates that *conventional scaled MOSFETs can operate as optical modulators*, by transforming the channel oxide into a plasmon slot waveguide.

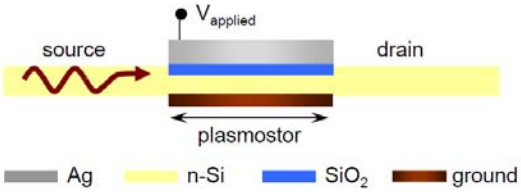

λ = 1550 nm (t_{Si}~170 nm)	|E| mode profile	Mode Index	Loss (dB/μm)
Off state ($V_{applied}$=0) *depletion*		3.641	0.207
		0.375	2.37
On state ($V_{applied}$>V_{FB}) *accumulation*	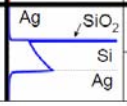	3.649	0.228
		0.033	28.14

Figure 3. Device schematic and tabulated mode properties of the plasmostor. Tabulated mode profiles, refractive indices and losses for the plasmostor in both depletion (voltage-off) and accumulation (voltage-on) states.

The accumulation-based operation of the plasmostor relies on cutoff of a photonic mode in the Si core. By designing the plasmostor with a 170-nm-thick Si core and 10-nm SiO_2 channel, a small gate voltage can cutoff the TM_2 photonic mode for wavelengths spanning λ = 1.48 μm to 1.58 μm. Plasmostor operation at λ =1.55 μm is illustrated in Figure 3. Here, the plasmostor is modelled as a four-layer waveguide consisting of semi-infinite Ag cladding layers surrounding the Si core and SiO_2 channel. In the off state (V=0), the unbiased plasmostor supports two modes: the TM_2 photonic mode lying to the left of the Si and SiO_2 light lines, and a plasmonic mode lying to the right of the Si light line.

As seen in the table of Figure 3, the photonic mode (red) is characterized by an electric field localized predominately in the Si core and a mode index of n=0.375. In contrast, the plasmonic mode (blue) exhibits maximal field intensities within the SiO_2 channel and a mode index of n=3.641. Losses of the plasmonic and photonic modes are 0.207 dB/_m and 2.37 dB/_m, respectively. For both modes, fields in the metal cladding decay within approximately 20 nm of the Ag-Si and Ag-SiO2 interfaces. Modifying the Si index through free-carrier absorption can push the TM_2 mode into cutoff, such that this modal dispersion curve intercepts the energy axis just above λ =1.55μm. The remaining plasmonic mode will then propagate through the plasmostor without interference from the photonic mode. In the plasmostor, such changes in the Si index are induced by applying a positive bias to the gate. For drive voltages above the flat-band voltage, electrons in the n-type Si form an accumulation layer characterized by a peak carrier concentration at the Si/SiO_2 interface and a spatial extent given by the Debye length. Figure 3 tabulates the theoretical change of mode index and propagation length with the onset of accumulation. Here, the accumulation layer is modeled as a multi-layer Drude electron gas with an average carrier concentration of approximately $5x10^{18}$ /cm^3 and a Debye decay length of 14 nm. As expected, the effective index and losses of

the plasmonic mode exhibit very little change between the voltage-off (depletion) and voltage-on (accumulation) states. In particular, the plasmonic mode index varies from the off state byΔn = 0.008, and losses are only slightly increased to 0.228dB/μm. However, the photonic mode is pushed into cutoff, as indicated by the near-zero mode index and substantially increased losses (i.e., the photonic mode becomes evanescent). Therefore, in the accumulation state, the plasmostor will guide near-infrared light almost exclusively through the 10-nm-thick SiO_2 channel, solely via the plasmonic mode. Finite-difference time-domain simulations of plasmostor operation are illustrated in Figure 6. In these simulations, the plasmostor is excited at 1.55 μm via a Si-waveguide. The plasmostor length has been set to 1.6 μm, and the transverse source and drain dimensions are equal to the plasmostor core thickness. This Si waveguide source supports a fundamental TM photonic mode that couples into the plasmostor with coupling efficiencies of ~ 30%. Note however that more efficient coupling schemes, exhibiting ~ 90% coupling efficiencies, are possible. As seen in the upper panel of Figure 4a, in the absence of an applied gate voltage, plasmostor fields are distributed throughout the Si core with sparse regions of high electric field in the oxide slot. However, with the onset of accumulation, the field transmitted within the Si core is notably decreased.

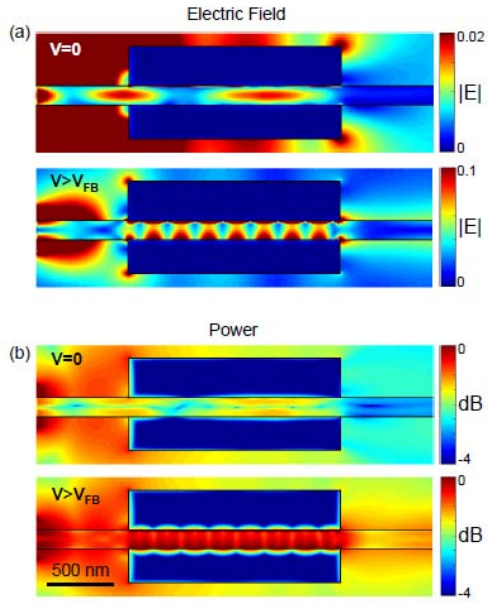

Figure 4. Finite difference time domain simulations of the plasmostor, showing the total electric field (a) and the transmitted power (b) for a 1.6-μm-long optical source drain separation. Plasmostor mode and power profiles at λ =1.55 μm are shown in both the voltage-off (depletion) and voltage-on (accumulation) states.

As seen in the lower panel of Figure 4a, plasmostor fields are localized predominately within the 10-nm-thick oxide layer and along the Si/Ag interface. In one sense, the oxide layer serves as an optical channel between the optical source and optical drain. Within the plasmostor, pronounced maxima and minima within the resonator can be observed with a wavelength of ~250 nm. By choosing the source-drain separation to correspond to a condition of destructive interference between the photonic and plasmonic mode, plasmostor transmission can be substantially increased by inducing accumulation. Figure 4b plots the total power transmitted through the plasmostor at l = 1.55 mm, with a source-drain separation d = 1.6 mm. Comparing intensities at the optical drain between the voltage-off and voltage-on states, modulation ratios of approximately +4 dB can be observed.

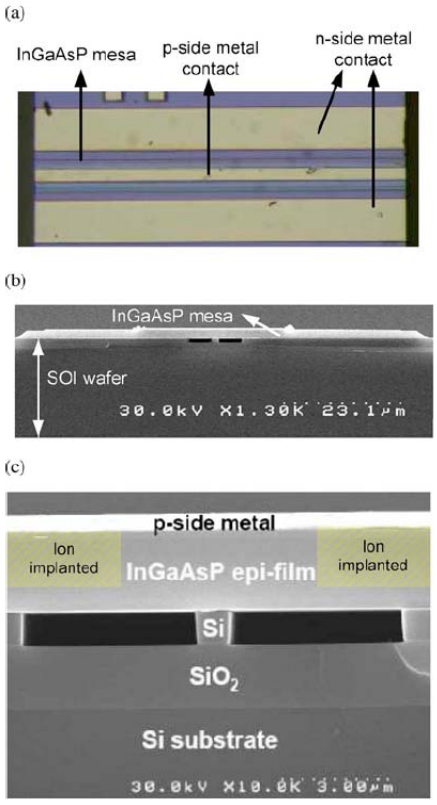

Figure 5. (a) Top view of a fabricated device. (b) SEM overview of a cross section of the device. (c) SEM close-up view of the device cross section at the Si waveguide region. Approximate ion implanted regions are superimposed on the image for illustration.

Electrically pumped hybrid evanescent Si/InGaAsP lasers

Working together with the groups of Amnon Yariv and Axel Scherer, we demonstrated an electrically-pumped hybrid Si/III–V, Fabry–Perot evanescent laser utilizing InGaAsP as the III–V gain material. The lasing threshold current of 300-mm-long devices was as low as 24 mA, with a maximal single facet output power of 4.2 mW at 15°C. Longer devices achieved a maximal single facet output power as high as 12.7 mW, a single facet slope efficiency of 8.4%, and a lasing threshold current density of 1 kA/cm^2. Continuous wave laser operation was obtained up to

45°C. The threshold current density, output power, and efficiency obtained improve upon those of previously reported devices having a similar geometry. Facet images indicate that the output light is largely confined to the Si waveguide.

Figure 5 shows a top view optical microscope image and scanning electron microscope (SEM) images of the device's cross section.

Figure 6(a) shows the output power and device voltage versus current (L–I–V curve) of a 960-μm long device, mounted on a thermoelectric cooler at 15°C. The turn-on voltage was 0.8 V, and the lasing threshold voltage V_{th} was 1.3 V. The threshold current *I*th was 60 mA, corresponding to a threshold current density J_{th} of 1.25 kA/cm^2. The maximum power output P_{max} from a single facet was 12.5 mW, and the differential slope efficiency for a single facet was 8.4%. The series resistance of the laser was 8 W. The inset of Fig. 6(a) shows I_{th} as a function of temperature. Continuous wave lasing was achieved at temperatures up to 45°C, and the characteristic temperature of the device was found to be 39°K. Figure 6(b) shows the laser spectrum, whose central wavelength was 1490 nm. The modal loss was estimated as 28 cm^{-1} below the bandgap . The measured value of differential slope efficiency corresponds to an internal quantum efficiency of 0.54. Values of J_{th} of 1–1.5 kA/cm^2 were obtained for numerous devices, having lengths ranging between 300 and 1500 mm. I_{th} of the 300-mm-long devices was 24 mA at 15°C, with P_{max} of 4.2 mW. J_{th} and V_{th} of the devices are about 35% lower than those of the previously reported FP hybrid Si/AlGaInAs lasers from John Bower's group. At the same time, our devices have a P_{max} which is 70% higher, and their differential slope efficiency is 30% higher.

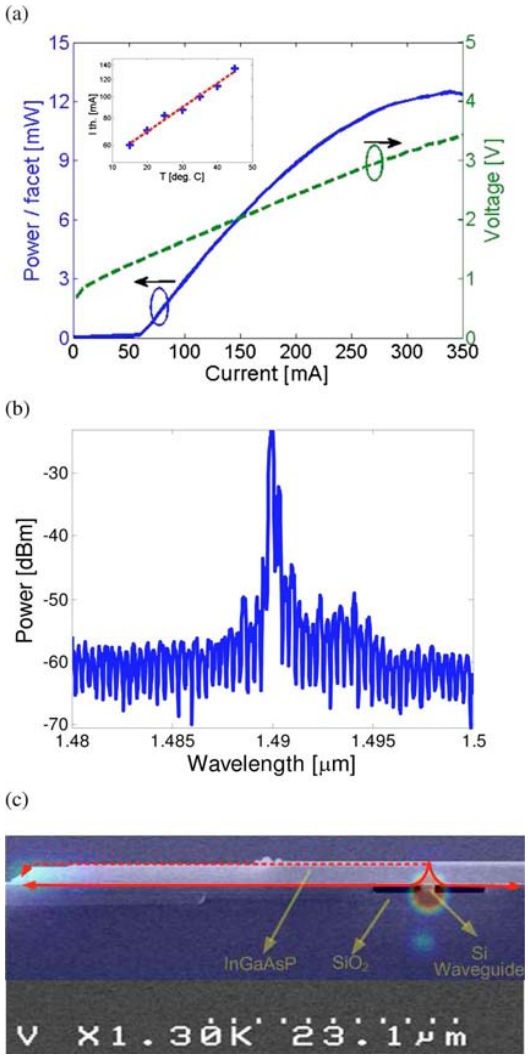

Figure 6. (a) L–I–V curve of a 960-μm-long laser under cw operation at 15°C. Inset, lasing threshold current (mA, log scale) as a function of temperature (°C) (+), alongside a linear fit (dashed line). (b) Laser spectrum, dB scale. (c) Image of the lasing mode, superimposed upon a scaled SEM cross-sectional view of the device. The solid lines indicate the main current paths from the *p* side towards the *n* side, as defined by the ion implantation. The dashed line indicates a residual leakage current path.

At this stage, we cannot yet determine whether the improved performance is due to the choice of gain material or due to other fabrication related differences. A high-resolution image of the laser beam is shown in Fig. 2(c), superimposed on a scaled SEM cross-sectional image of the device. The high-intensity beam overlaps the silicon waveguide. Another spot, whose intensity is 15% of that of the main beam, appears at the left-hand sidewall. Since the current confinement induced by the ion implantation is not complete, low residual currents may flow along the highly doped *p*-InGaAs layer towards the edge of the mesa, and then down towards the *n*-side contact. Although negligible in most devices, the current leakage was sufficient to generate the secondary beam in this specific example. Though generally undesirable, this beam was useful in the proper vertical alignment of the two images. Another weak spot below the silicon waveguide, whose intensity is 10% of that of the main beam, is due to a diffraction pattern. The image provides a striking illustration to the confinement of the lasing mode in the Si waveguide. Ongoing work focuses on the "supermode control" of the optical confinement along the laser cavity. Such control is expected to provide significant further improvement in device performance.

Personnel Supported:

Faculty: Dr. Harry A. Atwater
Postdocs: Domenico Pacifici (partial).
Graduate Students: Kenneth Diest (partial), Carrie Hofmann, Jennifer A. Dionne (partial)
Collaborators: Albert Polman, Axel Scherer, Amnon Yariv

Publications: Peer-reviewed publications submitted and/or accepted during the 12-month period starting the previous 1 October (or since start for new awards).

1. Quantitative determination of optical transmission through subwavelength slit arrays in Ag films: Role of surface wave interference and local coupling between adjacent slits
   Author(s): Pacifici, D; Lezec, HJ; Atwater, HA, et al.
   Source: **PHYSICAL REVIEW B** Volume: **77** Issue: **11** Article Number: **115411** Published: **2008**

2. Surface plasmon polariton modes in a single-crystal Au nanoresonator fabricated using focused-ion-beam milling, Vesseur, EJR; de Waele, R; Lezec, HJ, et al.,**APPLIED PHYSICS LETTERS 92** Article Number: 083110 **(** 2008).

3. Optical cavity modes in gold shell colloids, Penninkhof, JJ; Sweatlock, LA; Moroz, A, et al., **JOURNAL OF APPLIED PHYSICS 103** Article Number: **123105 (**2008).

4. Title: Loss mechanisms of surface plasmon polaritons on gold probed by cathodoluminescence imaging spectroscopy, Kuttge, M; Vesseur, EJR; Verhoeven, J, et al., **APPLIED PHYSICS LETTERS 93** Article Number: **113110 (**2008).

5. Special Issue on Surface Plasmon Photonics, H.A. Atwater, D.P. Tsai and J.R. Krenn, **IEEE JOURNAL OF SELECTED TOPICS IN QUANTUM ELECTRONICS, 14**, 1393(2008).

6. Title: Tunable Color Filters Based on Metal-Insulator-Metal Resonators, K. Diest, J. A. Dionne, M.Spain, and H.A. Atwater **NANO LETTERS 9,** 2579-2583 (2009).

7. Electrically pumped hybrid evanescent Si/InGaAsP lasers, Xiankai Sun, Avi Zadok,* Michael J. Shearn, Kenneth A. Diest, Alireza Ghaffari, Harry A. Atwater, Axel Scherer, and Amnon Yariv, **OPTICS LETTERS 34** 1345 (2009).

8. PlasMOStor: A Metal-Oxide-Si Field Effect Plasmonic Modulator, J.A. Dionne, K. Diest, L.A. Sweatlock, and H.A. Atwater, **NANO LETTERS 9,** 897-902(2009).

a. **Invited Conference and Seminar Presentations**

Listed below is a summary of the 16 invited presentations given on the subject of plasmonic materials and devices under this contract during the period 7/1/08-6/30/09:

2009

6/30/09 Invited Talk, ICMAT International Conference for Materials in Advanced Technologies, Singapore
6/23/09 Invited Talk, SPP4 4th International Conference on Surface Plasmon Photonics, Amsterdam
6/19/09 Plasmonics Seminar CEA-LETI, Grenoble, France
4/27/09 Physics Colloquium, Harvard University, Cambridge, MA
4/23/09 Chemistry Colloquium, Harvard University, Cambridge, MA
4/15/09 Invited Talk, Symposium I, Spring 2009 Materials Research Society Meeting, San Francisco, CA
4/15/09 Invited Talk, Symposium L, Spring 2009 Materials Research Society Meeting, San Francisco, CA
4/8/09 Chemistry Seminar, University of Southern California
3/23/09 Plenary Lecture, German Physical Society Spring Meeting, Dresden
3/19/09 Air Force Research Laboratory, Dayton, OH
3/17/09 American Physical Society, Invited Talk, APS March Meeting, Pittsburgh PA
3/15/09 American Physical Society, Frontiers in Energy Workshop, APS March Meeting, Pittsburgh PA
3/2/09 Innovative Solar Cell Workshop, University of Tokyo, Tokyo, Japan
2/20/09 Chemical Engineering and Materials Sciences Seminar, UC Irvine, Irvine, CA
1/28/09 Photonics West, San Jose, CA
1/23/09 Nanoscience Seminar, University of California at San Diego, La Jolla, CA
1/6/09 Plenary Lecture, NanoMeta, 2nd European Meeting on Nanophotonics and Metamaterials, Seefeld Austria

2008

12/5/08 Physical Sciences Seminar, IBM Research, Yorktown Heights, NY
12/2/08 Symposium N, Fall 2008 Materials Research Society Meeting, Boston, MA
12/2/08 Symposium RR, Fall 2008 Materials Research Society Meeting, Boston, MA
11/17/08 Nanofrontiers 2.0 National Academy of Sciences Workshop, Washington, DC
10/22/08 OSA "Plasmonics and Metamaterials 2008" Optics and Photonics Congress, Rochester, NY
9/3/08 Optical Metamaterials and Plasmonics Workshop, Estes Park, CO
8/26/08 Photon 08: Quantum Electronics and Photonics, Edinburgh, Scotland
7/15/08 Gordon Research Conference on Nanostructure Fabrication

b. **Consultative and Advisory Functions**

Atwater had advised Cynthia Daniell of DARPA STO on developments in plasmonic photovoltaics.

c. **Transitions**.

Jennifer Dionne has accepted a position as a member of the Stanford University faculty; she will take up this position after a brief postdoc in the laboratory of A. Paul Alivisatos at Berkeley.